



Impacts of landscape structure on surface urban heat islands: A case study of Shanghai, China

Junxiang Li ^{a,b,*}, Conghe Song ^c, Lu Cao ^a, Feige Zhu ^a, Xianlei Meng ^a, Jianguo Wu ^d

^a Department of Environmental Science, East China Normal University, Shanghai 200062, China

^b Shanghai Key Laboratory of Urbanization and Ecological restoration, East China Normal University, Shanghai 200062, China

^c Department of Geography, CB# 3220, 205 Saunders Hall, University of North Carolina at Chapel Hill, Chapel Hill, NC 27599, USA

^d School of Life Sciences and Global Institute of Sustainability, Arizona State University, Tempe, AZ 85287, USA

ARTICLE INFO

Article history:

Received 11 January 2011

Received in revised form 6 June 2011

Accepted 9 July 2011

Available online 5 August 2011

Keywords:

Urban heat island

Spectral mixture analysis

Vegetation fraction

Impervious surface

NDVI

Landscape metrics

Shanghai

ABSTRACT

Urbanization is taking place at an unprecedented rate around the world, particularly in China in the past few decades. One of the key impacts of rapid urbanization on the environment is the effect of urban heat island (UHI). Understanding the effects of landscape pattern on UHI is crucial for improving the ecology and sustainability of cities. This study investigated how landscape composition and configuration would affect UHI in the Shanghai metropolitan region of China, based on the analysis of land surface temperature (LST) in relation to normalized difference vegetation index (NDVI), vegetation fraction (Fv), and percent impervious surface area (ISA). Two Landsat ETM+ images acquired on March 13 and July 2, 2001 were used to estimate LST, Fv, and percent ISA. Landscape metrics were calculated from a high spatial resolution (2.5×2.5 m) land-cover/land-use map. Our results have showed that, although there are significant variations in LST at a given fraction of vegetation or impervious surface on a per-pixel basis, NDVI, Fv, and percent ISA are all good predictors of LST on the regional scale. There is a strong negative linear relationship between LST and positive NDVI over the region. Similar but stronger negative linear relationship exists between LST and Fv. Urban vegetation could mitigate the surface UHI better in summer than in early spring. A strong positive relationship exists between mean LST and percent ISA. The residential land is the biggest contributor to UHI, followed by industrial land. Although industrial land has the highest LST, it has limited contribution to the overall surface UHI due to its small spatial extent in Shanghai. Among the residential land-uses, areas with low- to middle-rise buildings and low vegetation cover have much high temperatures than areas with high-rise buildings or areas with high vegetation cover. A strong correlation between the mean LST and landscape metrics indicates that urban landscape configuration also influences the surface UHI. These findings are helpful for understanding urban ecology as well as land use planning to minimize the potential environmental impacts of urbanization.

© 2011 Elsevier Inc. All rights reserved.

1. Introduction

More than 50% of the world's population now live in urban areas, and this number will continue to increase, particularly in developing countries (United Nations, 2008). Urbanization profoundly influences biodiversity and ecosystem functions, as well as local and regional climate and the quality of life (Luck and Wu, 2002). One of the ecological consequences of urbanization is the urban heat island (UHI) effect, which leads to higher temperature in urban area than surrounding suburban/rural areas. UHI can be evaluated in two ways. Traditionally, it is derived from air temperature measurements within the urban canopy layer. Recently, more studies of UHI are based on surface radiative temperature from remote sensors (Voogt, 2002).

Accordingly, the remotely sensed UHI has been termed the surface urban heat islands (SUHI) (Streutker, 2002). One important advantage of using remotely sensed surface temperature is its wall-to-wall coverage of the urban area, explicitly revealing its spatial patterns, although it only provide an instantaneous measurement of temperature during the day. In the earlier stage, NOAA-AVHRR data were used to derive land surface temperatures (LST) for UHI studies (Balling and Brazel, 1988; Gallo et al., 1993; Roth et al., 1989; Streutker, 2002, 2003). Recently MODIS data was used to study the SUHI (Cheval and Dumitrescu, 2009; Tran et al., 2006). However these data with 1 km spatial resolution were suitable only for coarse-scale urban temperature mapping, not for establishing accurate and meaningful relationships between image-derived values and those measured on the ground (Weng and Quattrochi, 2006; Weng et al., 2004). The availability of LST from Landsat with a spatial resolution of 120–60 m has significantly facilitated the study of the relationship between SUHI and surface biophysical parameters (Nichol, 1994,

* Corresponding author at: Department of Environmental Science, East China Normal University, Shanghai 200062, China. Tel./fax: +86 21 6223 7885.

E-mail address: jxli@des.ecnu.edu.cn (J. Li).

1996, 1998; Weng, 2001; Weng et al., 2006, 2004; Yuan and Bauer, 2007).

Vegetation and impervious surface are two key urban components as reflected in the VIS (Vegetation-Impervious surface-Soil) conceptual model of urban structure (Ridd, 1995). Vegetation transpiration mitigates the effect of UHI, and thus numerous studies have focused on understanding the relationship between LST and NDVI (Carlson et al., 1994; Gillies et al., 1997; Goward et al., 2002; Lo et al., 1997; Weng, 2001). However, NDVI suffers from the nonlinearity with vegetation abundance, platform tendency, and other interference of background conditions (Sandholt et al., 2002; Small, 2001). Weng et al. (2004) found that urban LST was more strongly related to vegetation fraction than NDVI. Yuan and Bauer (2007) found that the NDVI–LST relationship was more suitable for the analysis of UHI in summer and early autumn. While these findings were based on regional trends, there are tremendous spatial–temporal variations within the general trend. These variations are not yet well understood.

Urban landscapes are characterized by complex spatial heterogeneity, with different Land-cover/land-use (LCLU) types having their own surface characteristics and forming patch mosaics (Wu, 2008; Wu et al., 2011). Cities' spatial pattern can affect physical, ecological, and socioeconomic processes within their boundaries and beyond (Luck and Wu, 2002). Therefore it is necessary to relate the spatial pattern of urbanization to ecological processes to help better understand the urban ecosystems (Luck and Wu, 2002; Turner, 2005). To enhance the understanding of the relationship between urban thermal behavior and urban landscape structure, Voogt and Oke (2003) suggested to better quantify appropriate surface radiative (e.g. emissivity) and structural parameters from remote sensing. More recently, Weng et al. (2007) and Liu and Weng (2008) assessed the relationship between LCLU and landscape metrics by LST zones. Buyantuyev and Wu (2010) studied UHI and landscape heterogeneity by linking spatiotemporal variations in surface temperatures to land-cover and socio-economic patterns and found that vegetation and pavements were key factors for the spatial variations of surface temperature. However, how urban landscape structure influence urban LST has not been fully understood.

The main objective of our study was to investigate how different urban landscape features and their spatial configuration affect UHI, and how these relationships compare and contrast between the leaf-on and leaf-off seasons. Our study was carried out in Shanghai, China, a major international metropolis that has experienced rapid development since China adopted the reform and opening-up policies in recent decades. Understanding the spatiotemporal pattern of UHI and its drivers in Shanghai has important implications for many other coastal cities around the world.

2. Methods

2.1. Study area

The Shanghai metropolitan region, situated on the broad flat alluvial plain of the Yangtze River Delta of China, covers a total area of approximately 6340.5 km², with a few remnant hills in the southwest (Fig. 1). Shanghai locates in the northern subtropical monsoon climate with a mean annual temperature of 16.0 °C (from minimum 12.7 °C to maximum 20.2 °C), and a mean annual precipitation of 1158.1 mm (data calculated from the observation of 1951 to 2008), and with an average elevation of about 4 m above the sea level, the area has thousands of streams and rivers. Among them, Huangpu River is the biggest one, which runs through the urban center. Native vegetation is characterized by the subtropical evergreen broadleaved forest and the evergreen broadleaved-deciduous broadleaved mixed forest. As the largest city in China, Shanghai has experienced enormous urbanization in both scope and intensity, driven by rapid economic development, particularly, since the 1990s. Shanghai has a population of more than 19.21 million, and its GDP reached 1504.6 billion Yuan

(~US\$215 billion) in 2009 (Shanghai Municipal Statistics Bureau, 2010). Thus, Shanghai metropolitan area has become the engine of the economic growth for the Yangtze River Delta region. Our study focused on the area enclosed by the outmost ring-road, which encloses about 665.5 km² with diverse LCLU types as can be seen in Fig. 1 and Table 1.

2.2. Images and image pre-processing

Two cloud-free Landsat-7 Enhanced Thematic Mapper Plus (ETM+) images (Row/Path: 038/118), which were collected on 13 March 2001 and 03 July 2001, respectively, were acquired from USGS EDC. The images were further rectified to the Universal Transverse Mercator project system (datum WGS84, UTM Zone N51), and resampled using the cubic convolution algorithm with a pixel size of 30 by 30 m for all bands. The root mean squared errors were smaller than 0.25 pixels (7.5 m) for each of the two images. The overall image processing and data analysis steps are shown in Fig. 2.

Calculation of at-sensor spectral radiance is a fundamental step in converting image data from multiple sensors and platforms into a physically meaningful common radiometric scale. We converted the Digital Numbers (DN) for both reflective and thermal bands to at-sensor radiance using the following equation (Chander and Groeneveld, 2009):

$$L_{\lambda} = \frac{(LMAX_{\lambda} - LMIN_{\lambda})}{(Q_{calmax} - Q_{calmin})} \times (Q_{cal} - Q_{calmin}) + LMIN_{\lambda} \quad (1)$$

where L_{λ} is the spectral radiance at the sensor's aperture in $W/(m^2 sr \mu m)$, Q_{cal} the quantized calibrated pixel value [DN], Q_{calmin} the minimum quantized calibrated pixel value corresponding to $LMIN_{\lambda}$ [DN], Q_{calmax} the maximum quantized calibrated pixel value corresponding to $LMAX_{\lambda}$ [DN], $LMIN_{\lambda}$ the spectral at-sensor radiance scaled to Q_{calmin} in $W/(m^2 sr \mu m)$, and $LMAX_{\lambda}$ the spectral at-sensor radiance scaled to Q_{calmax} in $W/(m^2 sr \mu m)$.

For image-based atmospheric correction, uniform atmospheric condition is usually assumed (Song et al., 2001), thus the correction will not have an effect on the analysis in this paper. Therefore for all the reflective bands, we used top-of-atmosphere (TOA) reflectance, which corrects for the cosine effect of solar zenith angles, and changes in the exoatmospheric solar irradiance due to variation in the earth–sun distance. These variations can be significant geographically and temporally (Chander and Groeneveld, 2009). We computed the TOA reflectance according to the following equation:

$$\rho_{\lambda} = \frac{\pi \cdot L_{\lambda} \cdot d^2}{ESUN_{\lambda} \cdot \cos\theta_s} \quad (2)$$

where ρ_{λ} is the planetary TOA reflectance [unitless], L_{λ} the spectral radiance at the sensor's aperture in $W/(m^2 sr \mu m)$, d the earth–sun distance [in astronomical unit], $ESUN_{\lambda}$ the mean exoatmospheric solar irradiance in $W/(m^2 \mu m)$, and θ_s the solar zenith angle.

The LCLU data used for sampling and impervious surface estimation were derived from 1:50,000 color-infrared aerial photos acquired from March to May, 2000. The aerial photos were scanned, registered to local coordinate systems, and then mosaicked for digitalization with GIS at the spatial resolution of 2.5 m. LCLU types derived from the airphotos were reclassified to eight broad categories as shown in Table 1 below. To facilitate further analysis, residential land use type has been further classified into 14 subtypes according to their height (building stories) and vegetation coverage. They are LRO: Low-rising old and humble house with vegetation cover less than 10%; LRR: Low-rising rural house (less than 3 stories); LR-1: Low-rising house (less than 7 stories) with vegetation cover less than 10%, LR-2: Low-rising house with vegetation cover between 10 and 30%, LR-3: Low-rising house with vegetation cover between 30 and 50%, LR-4: Low-rising house with vegetation cover over 50%; HR-1: High-rising house (7–18 stories)

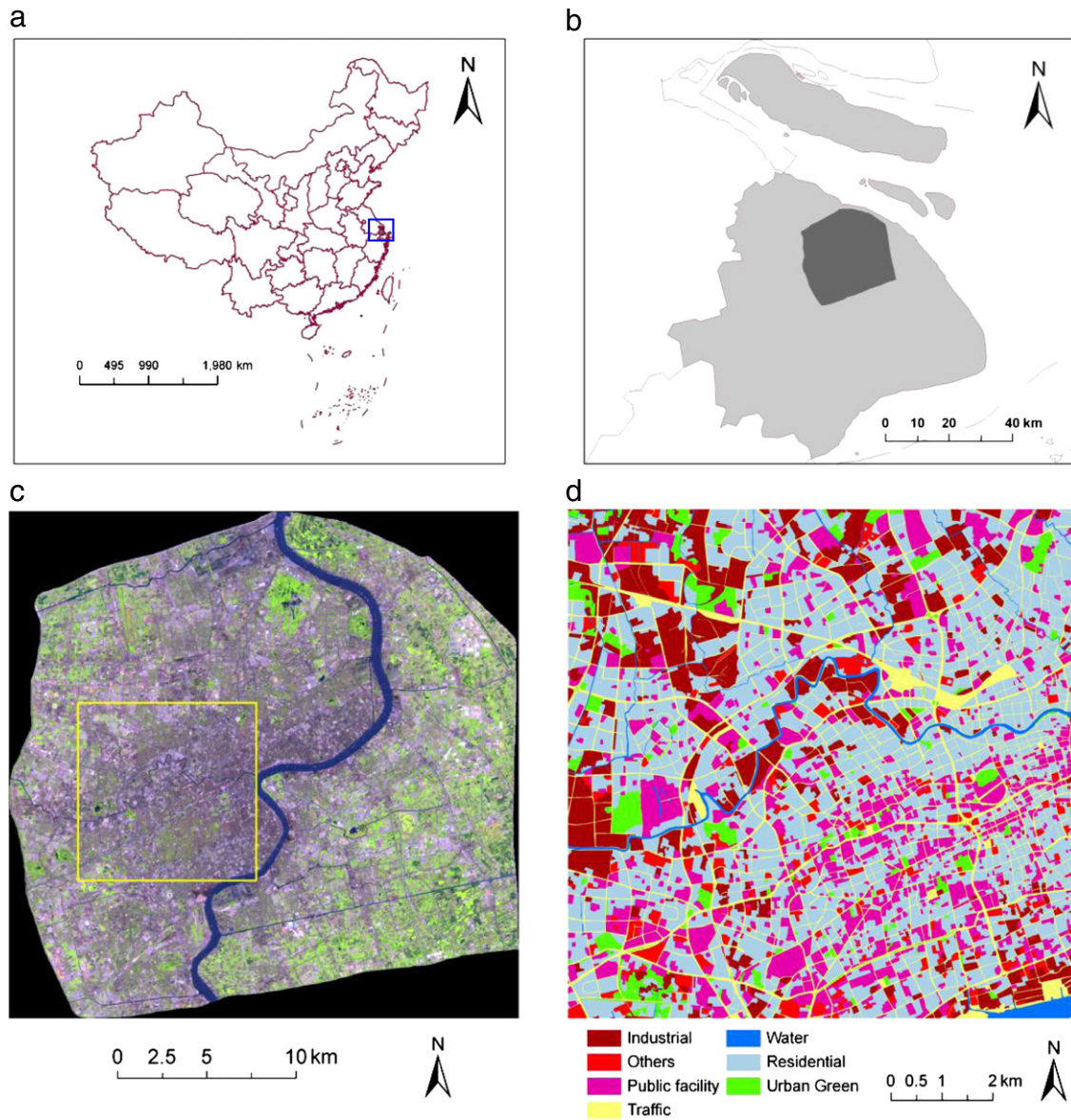


Fig. 1. Our study area: (a) Location of Shanghai in China; (b) Administrative boundary of Shanghai; (c) Our study area including Shanghai city proper as seen in the 03 July, 2001 Landsat-ETM+ image (RGB = 543); (d) land use map of a 10 × 10 km sample plot with spatial resolution of 2.5 × 2.5 m derived from aerial photos.

with vegetation cover less than 10%, HR-2: High-rising house with vegetation cover between 10 and 30%, HR-3: High-rising house with vegetation cover between 30 and 50%, HR-4: High-rising house with green cover over 50%; SR-1: Superhigh-rising house (over 18 stories) with vegetation cover less than 10%, SR-2: Superhigh-rising house with vegetation cover between 10 and 30%, SR-3: Superhigh-rising house with vegetation cover between 30 and 50%, SR-4: Superhigh-rising house with vegetation cover over 50%, respectively.

2.3. Estimating land surface temperature

Landsat ETM+ thermal infrared band (10.4–12.5 μm) data were utilized to map LST. This was accomplished in three steps: (1) converting calibrated DN to absolute units of at-sensor spectral radiance; (2) converting at-sensor spectral radiance to at-sensor brightness temperature; and (3) converting at-sensor brightness temperature to kinetic temperature, namely, land surface temperature (Barsi et al., 2003; Chander and Markham, 2003; Chander et al., 2009).

We carried out the first step using Eq. (1). Conversion of the at-sensor spectral radiance to at-sensor brightness temperature assumes that the earth’s surface is a black body (i.e., spectral emissivity is 1). The conversion formula is (Chander et al., 2009):

$$T_B = \frac{K_2}{\ln\left(\frac{K_1}{L_\lambda} + 1\right)} \quad (3)$$

where T_B is the effective at-sensor brightness temperature in Kelvin, L_λ is the spectral radiance at the sensor’s aperture in $W/(m^2 sr \mu m)$, and K_1 and K_2 are the pre-launch calibration constants. For Landsat ETM+, K_1 is 666.09 $W/(m^2 sr \mu m)$ and K_2 is 1282.71 K.

The brightness temperature values obtained above are referenced to a black body. Corrections for spectral emissivity (ϵ) of a greybody were made, and the emissivity-corrected land surface temperatures (T_s) were computed as follows (Artis and Carnahan, 1982):

$$T_s = \frac{T_B}{1 + (\lambda \times T_B / \alpha) \ln \epsilon} \quad (4)$$

Table 1
Urban land cover and land use classification system.

Level 1	Level 2
1 Residential	11 Urban and town residential
	12 Rural residential
2 Public facility	21 Municipal administration
	22 Commercial and financial services
	23 Cultural and sports services
	24 Hospital and sanitary
	25 Education and research institutes
	26 Civic utilities
3 Industrial	31 Light pollution industry such as electronic manufacture, tailoring industry, artware manufacture, etc.
	32 Middling pollution industry such as food industry, pharmaceutical industry, textile industry, etc.
	33 Heavy pollution industry such as metallurgical industry, chemical industry, machine manufacturing industry, paper industry, leather industry, etc.
	34 Warehouse
4 Traffic	41 Railroad
	42 Road and plaza
	43 Harbor and port
	44 Airport
	45 Other traffic land
5 Green land	51 Urban park
	52 Forest
	53 Shrub
	54 Grass land
	55 Botanic garden and zoo
	56 Natural reserves
	57 Greens in rural and country
	58 Other green land
6 Water	61 Streams and canals
	62 Lakes and reservoirs
	63 Ponds and aquafarms
	64 Beaches and wetland
7 Agricultural	71 Crop lands
	72 Vegetable fields
	73 Orchards
	74 Nurseries
	75 Other agricultural land
8 Others	81 Under-construction sites
	82 Specific land
	83 Cemetery
	84 Human historic relics
	85 Natural historic relics
	86 The others

where λ is the wavelength of emitted radiance (which is $11.5 \mu\text{m}$ according to Markham and Barker (1985)), $\alpha = hc/b$ ($1.438 \times 10^{-2} \text{ m K}$), b the Boltzmann constant ($1.38 \times 10^{-23} \text{ J/K}$), h the Planck's constant ($6.626 \times 10^{-34} \text{ Js}$), c the velocity of light ($2.998 \times 10^8 \text{ m/s}$), and ε the surface emissivity.

There are several methods to obtain the land surface emissivity, including the temperature/emissivity separation (TES) method (Gillespie et al., 1998) and the emissivity classification scheme (Snyder et al., 1998) if one has the detailed LCLU map. Here we employed an alternative and easy-to-apply approach to obtain land surface emissivity (ε) reported by Sobrino et al. (2004):

$$\varepsilon = \varepsilon_v F_v + \varepsilon_u (1 - F_v) + d\varepsilon \quad (5)$$

where ε_v is the emissivity of vegetation, ε_u is the emissivity of urban surface, and F_v is the vegetation proportion which was derived from an empirical model based on NDVI in Sobrino et al. (2004). We used the fractional vegetation cover for F_v derived from spectral mixture analysis as described in Section 2.4, and estimated $d\varepsilon$ by the equation from Sobrino et al. (2004):

$$d\varepsilon = (1 - \varepsilon_u)(1 - F_v)F\varepsilon_v \quad (6)$$

where F is a shape factor (Sobrino et al., 1990) whose mean value is 0.55, considering different geometrical distributions.

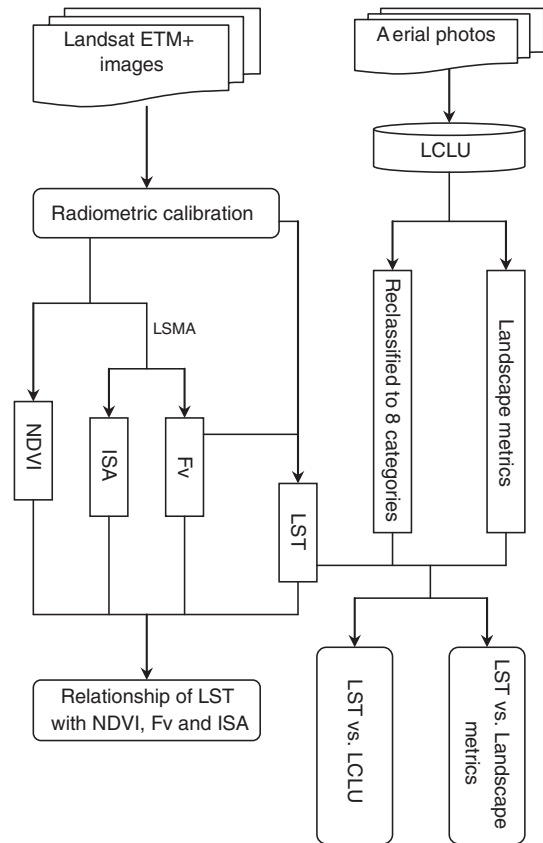


Fig. 2. Flowchart of data processing.

The emissivity of vegetation is typically 0.99, and the emissivity of urban surface (non-vegetation surface) is 0.92 according to previous studies (Artis and Carnahan, 1982; Nichol, 1998, 2009). The final expression for the emissivity is given by:

$$\varepsilon = 0.02644F_v + 0.96356 \quad (7)$$

Based on the steps above, we derived the LST map of the study area shown as Fig. 3-a, b.

2.4. NDVI, impervious surface fraction and vegetation fraction calculation

NDVI for Landsat ETM+ imagery was calculated as:

$$\text{NDVI} = \frac{\rho_{\text{nir}} - \rho_{\text{red}}}{\rho_{\text{nir}} + \rho_{\text{red}}} \quad (8)$$

where ρ_{nir} and ρ_{red} are the reflectance values in the near-infrared and red bands.

The NDVI maps for the study area are shown as Fig. 3-c, d. Impervious surface area (ISA) refers to the area that can neither evaporate water nor permit rainwater to penetrate (Carlson and Traci Arthur, 2000). Several methods have been developed in the literature to estimate ISA based on remotely sensed imagery (Yang and Liu, 2005). One is pixel-level estimation of ISA with traditional classification methods, such as the clustering algorithm (Deguchi and Sugio, 1994) and Maximum likelihood classification (Hodgson et al., 2003). The other is subpixel-level estimation using spectral mixing models (Ji and Jensen, 1999; Phinn et al., 2002; Wu, 2004; Wu and Murray, 2003), artificial neural networks (Civco et al., 2002; Hu and Weng, 2009), and classification trees (Goetz et al., 2003; Yang et al., 2003). Spectral mixture analysis is an advanced image processing method that determines the fraction of fundamental components, called endmembers, contained in each pixel

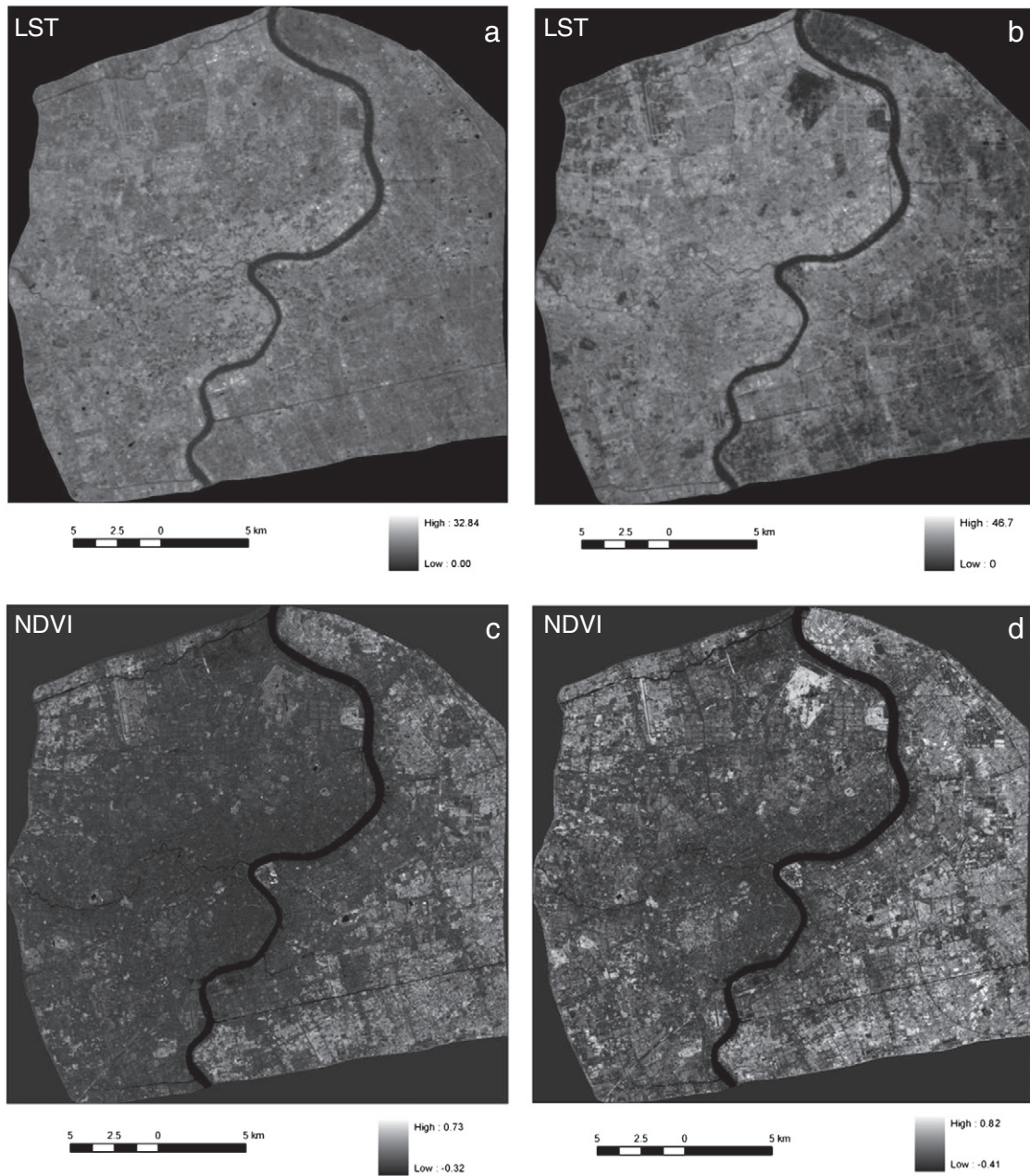


Fig. 3. Land surface temperature (LST) and normalized difference vegetation index (NDVI) derived from Landsat ETM+ images for the study area on two dates: a and c: Mar. 13, 2001; b and d: Jul. 3, 2001.

of an image (Yuan and Bauer, 2007). Here we utilized a normalized spectral mixture analysis (NSMA) method proposed by Wu (2004) to derive the impervious surface fraction. In this method, the normalization process was used to reduce the spectral variation due to brightness differences in the original spectra of urban components, using the following equation:

$$\bar{R}_b = \frac{R_b}{\mu} \times 100 \tag{9}$$

$$\mu = \frac{1}{N} \sum_{b=1}^N R_b \tag{10}$$

where \bar{R}_b is the normalized reflectance for band b in a pixel, R_b is the original reflectance for band b , μ is the average reflectance for that pixel, and N is the total number of bands (6 for ETM+ image).

Then a constrained linear spectral mixture analysis (LSMA) method was applied to quantify the urban surface composition in each pixel of the image using pure land covers (i.e., endmembers) as follows:

$$\bar{R}_b = \sum_{i=1}^m \bar{f}_i \bar{R}_{i,b} + e_b \tag{11}$$

where \bar{f}_i is the fraction of endmember i , $\sum_{i=1}^m \bar{f}_i = 1$ and $\bar{f}_i \geq 0$; $\bar{R}_{i,b}$ is the normalized reflectance of endmember i in band b for that pixel; m is the number of endmembers; and e_b is the residual. The fraction of each land cover type in a pixel was calculated using a least squares method in which the residual e_b was minimized.

In the LSMA model, the urban land cover endmembers generally are made up of vegetation, impervious surface, soil, and water (often masked out), or vegetation, high albedo (e.g. concrete, clouds, and

sand), low albedo (e.g. water and asphalt), and soil. Endmember spectral signatures are extracted from representative homogeneous pixels in the TM/ETM+ imagery when field or laboratory-based measurements of endmembers' spectra are not available (Wu, 2004; Wu and Murray, 2003). In this study, the Principal Component (PC) transformation was utilized to process the normalized reflectance of ETM+ imageries, and then visual interpretation of the ETM+ image was performed to select endmembers. Three endmembers of vegetation, high albedo and low albedo were identified from the feature space of PC1, PC2 and PC3 components. The soil endmember could not be found in our study area because of the lack of bare soil.

The high albedo and low albedo endmembers cannot be directly interpreted as impervious surfaces. But impervious surfaces also can be a linear combination of high albedo and low albedo expressed as follows (Wu and Murray, 2003):

$$R_{IS,b} = f_L R_{L,b} + f_H R_{H,b} + e_b \quad (12)$$

where $R_{IS,b}$ is the reflectance spectra of impervious surfaces for band b , and f_L and f_H are the fractions of low albedo and high albedo, respectively. $R_{L,b}$ and $R_{H,b}$ are the reflectance spectra of low albedo and high albedo for band b , and e_b is the residual. In Eq. (12), the constrained requirement is $f_L + f_H = 1$ and $f_L, f_H \geq 0$. The details of the LSMA and justification of endmember selection can be found in Wu (2004) and Wu and Murray (2003). The accuracy of the estimated fraction impervious surface (converted to percent impervious surface area, or %ISA) and fraction vegetation cover (F_v) was tested with randomly selected 220 samples of 3×3 pixel size (90×90 m) from a high resolution (2.5 m) land use database. For %ISA, the root mean square error (RMSE) and system error (SE) were 15.8% and 1.6% for July 3, 2001 and 11.3% and 3.7% for March 13, 2001. For F_v , the RMSE and SE were 10.7% and 2.1% for July 3, 2001 and 16.1%, 2.2% for March 13, 2001. The derived percent ISA and F_v map were shown as Fig. 4.

2.5. Landscape metric selection and calculation

It was demonstrated that land surface temperature or surface urban heat island could be related to LCLU types (Chen et al., 2006; Weng, 2001; Xian and Crane, 2006), and there are relationship between spatial structure of urban thermal patterns and urban surface characteristics (Liu and Weng, 2008; Weng et al., 2007). In the past few decades, a large number of landscape metrics have been developed and widely used to characterize landscape patterns (Gustafson 1998; Li and Reynolds, 1993; Li and Wu, 2004; McGarigal and Marks, 1995; O'Neill et al., 1988; Turner and Gardner, 1991; Wu, 2000; Wu et al., 2002) and to relate landscape patterns to ecological processes (Turner, 2005). These metrics fall into two general categories to measure the composition and spatial configuration (Gustafson 1998; McGarigal and Marks, 1995). Landscape composition metrics measure the presence and amount of different patch types within the landscape, without explicitly describing its spatial features (i.e., percentage land of a certain cover). Landscape configuration metrics measure the spatial distribution of patches within the landscape (i.e., degree of aggregation and contagion) (Alberti, 2005). We selected eight commonly used landscape metrics to relate land surface temperature with landscape patterns. They are given in Table 2 (for detailed calculation equation and comments, see McGarigal et al., 2002). They are selected to provide complementary information about landscape structure for both composition and configuration.

The landscape structure analysis is based on the highest spatial resolution data we have, 2.5×2.5 m air photos. Landscape metrics were computed both at the class and the landscape levels (Alberti, 2005; Herold et al., 2003, 2002). Due to the large amount of data involved, it is impractical to perform landscape metrics analysis using the air photos for the whole city. Therefore, we took a subset of

10×10 km sample plot (Fig. 1-d), which was carefully chosen so that it is representative of the city landscape structure. We divided the 10×10 km plot into 25 subplots of 2×2 km in size so that a statistical relationship could be developed using each subplot as a data point. The landscape metrics were computed with FRAGSTATS (McGarigal et al., 2002). When computing the landscape metrics for a class, all other classes within a subplot were masked out as background. For the landscape metric at the landscape level, all classes were considered within each subplot. Pearson's correlation coefficients between landscape metrics and the subplot mean LST were calculated. The significance of each correlation coefficient was determined using a two-tailed Student's t -test.

2.6. Statistical analysis

Regression analysis was used to further quantify the relationship among LST, NDVI, F_v , and percent ISA. The zonal analysis method (Yuan and Bauer, 2007) was used to evaluate the mean LST at each 0.01 increment of the NDVI from -1 to 1 , at each 0.01 increment of the F_v from 0 to 1 , and at each 1% increment of percent ISA from 0 to 100% . At each increment of NDVI, F_v , and percent ISA, a mean LST value was obtained from all corresponding pixels. These relationships are scale dependent. According to Woodcock and Strahler (1987), the optimal spatial resolution to capture spatial pattern using remotely sensed imagery is approximately half to three-quarters of the size of the object dimension in the scene. Weng et al. (2004) performed an analysis on the scale effect on monitoring UHI using remote sensing and found that 60×60 m spatial resolution is approximately the optimal spatial resolution. Therefore, we performed the analyses at the finest spatial scale as the data allowed, which was appropriate to capture the spatial features of UHI and relevant land use and land cover types.

3. Results

3.1. Relationship of LST to NDVI and vegetation fraction

The relationship between LST and NDVI of early spring (March 13, 2001) and the summer (July 3, 2001) images are shown in Fig. 5-a, b. As the study area is located in the northern subtropical region, there is a fair amount of active vegetation in the early spring. Thus, mean NDVI is relatively high in the early spring (0.10 ± 0.1) compared to that for the summer (0.20 ± 0.16). The mean NDVI is low overall for the city as a result of the abundance of impervious surface. The shape of the scattergram changes significantly from the early spring to summer because of the significant increase in temperature and NDVI in the summer. The upper edge and lower edge of the triangle scattergram (Fig. 5-a, b) have been termed as "warm edge" and "cool edge", respectively, in previous studies (Carlson and Traci Arthur, 2000; Carlson et al., 1995; Gillies and Carlson, 1995; Gillies et al., 1997). The pixels with same NDVI value are warmer and drier near warm edge than those near cool edge. The two edges converge well at high NDVI end for the early spring image. The warm edges in both images have negative slopes, indicative of the cooling effect of vegetation. This is primarily due to the effect of high energy demand for vegetation transpiration; while the cool edge has a positive slope for the early spring image and remains negative for the summer image. Therefore, the role of vegetation in regulating the land surface temperature varies with season.

On the regional basis, NDVI has a highly nonlinear relationship with mean LST over the whole range of NDVI values. But a strong negative linear relationship exists between mean LST and positive NDVI, i.e. with the presence of vegetation (Fig. 6-a, b). The regression lines in Fig. 6-a, b between NDVI and mean LST are based on positive NDVI only. It is interesting to note that there is an enhanced variation in the relationship between NDVI and LST at high NDVI, particularly in the summer time. Similar trend was found in the studies by Chen et al.

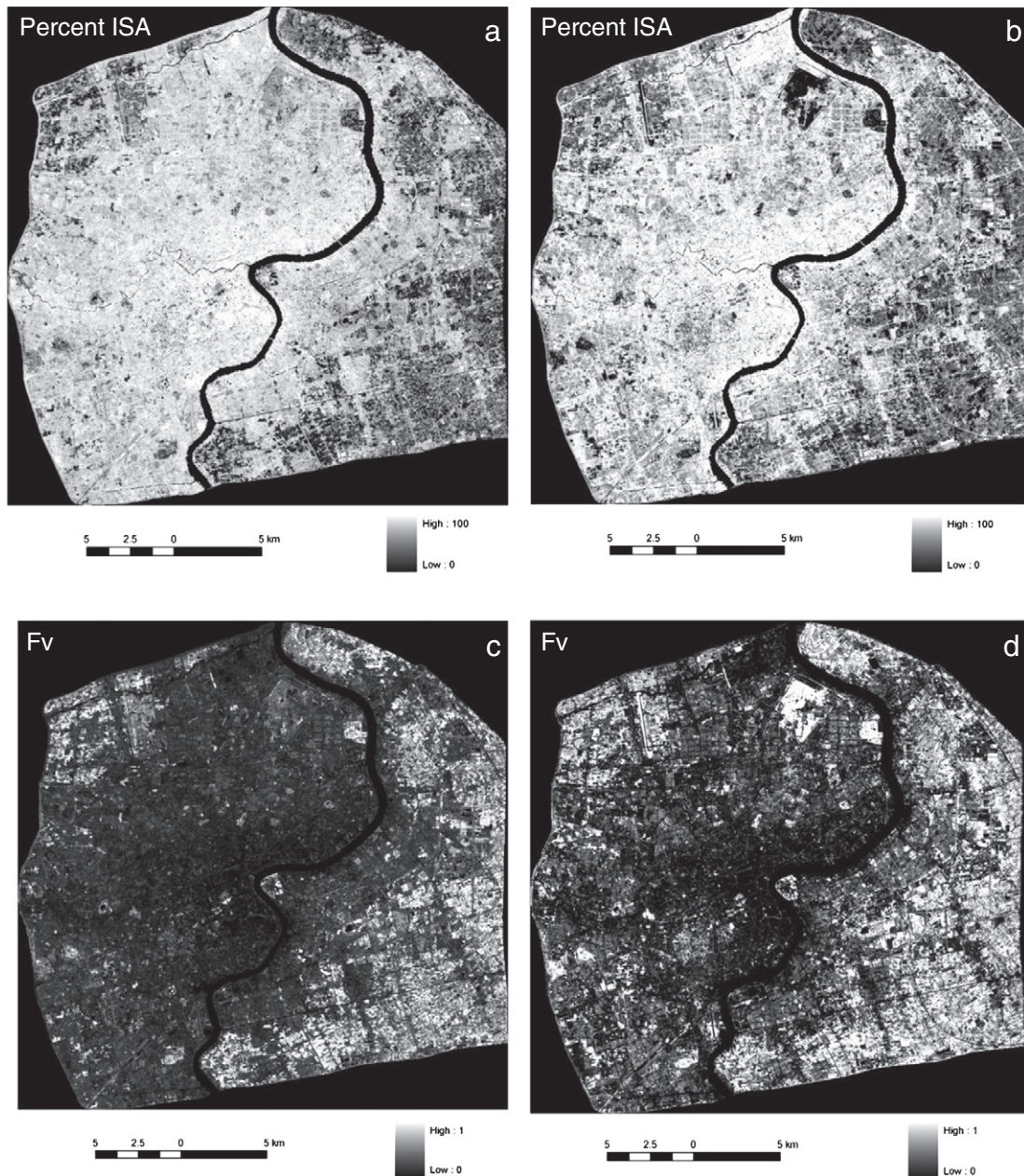


Fig. 4. Percent impervious surface area (ISA) and fractional vegetation cover (Fv) derived from Landsat ETM+ image for the study area on two dates: a and c: Mar. 13, 2001; b and d: Jul. 3, 2001.

(2006) and Yuan and Bauer (2007). These pixels are nearly completely covered by vegetation. This phenomenon may be caused by any of the following three processes: (1) NDVI is saturated with leaf area index (LAI). Further increase in LAI will not lead to increase in NDVI, but higher LAI leads to cooler surface temperature due to the effect of higher evapotranspiration, and vice versa. (2) Vegetation type may also cause the NDVI-LST to scatter at high NDVI at the regional scale. According to our field observations in the summer 2010 (unpublished data), the LST difference between tree/grass mixed types and lawns varies from 0.1 °C to 9.3 °C with an average difference as high as 4.0 °C, and similar difference was observed for tree/shrub mixed types with lawns. (3) Development density influences the surface temperature of vegetation. For example, street trees with higher NDVI value in dense urban development areas, especially in dense urban street canyons, have higher surface temperature. We found that surface temperatures of golf lawn and street trees are approximately 3.0 °C and 4.0 °C higher than those of park forest with the same NDVI value, respectively, based on the 03 July 2001 image.

Another land surface biophysical parameter often used to represent vegetation abundance is Fv, which is closely related to NDVI. Because NDVI can saturate at high Fv when the background is dark (Song, 2004), Fv is a more accurate representation of vegetation abundance. The pixel-based and regional-based relationships between LST and Fv in the early spring and the summer are shown in Figs. 5-c, d and 6-c, d, respectively. Fv has a slightly stronger relationship with LST than NDVI, especially in summer ($R^2 = 0.9957$). But variations with seasons exist.

3.2. LST relationship with percent impervious surface

Given that both NDVI and vegetation fraction vary with seasons, we investigated the relationship between LST and ISA (Fig. 5-e, f). LST generally increased with percent ISA, opposite to the pattern between vegetation abundance and LST because ISA and vegetation fraction are mutually exclusive endmembers in our LSMA. High vegetation fraction means low percent ISA. The variation of LST increased with percent ISA, and significantly higher variations in LST occurred for

Table 2
Landscape pattern metrics used in this study, after McGarigal et al. (2002).

Landscape metrics	Calculation and description
<i>Compositional</i>	
Percentage of Landscape area (PLAND)	$PLAND_i = P_i = 100 \times \frac{\sum_{j=1}^n a_{ij}}{A}$ <p>P_i is proportion of the landscape occupied by patch type (class) i; and n is the number patches in the landscape for class i; a_{ij} is the area of patch ij. A is the total landscape area. It is a measure of landscape composition.</p>
Shannon's Evenness Index (SHEI)	$SHEI = - \frac{\sum_{i=1}^m (P_i \times \ln P_i)}{\ln(m)}$ <p>P_i is proportion of the landscape occupied by patch type (class) i; m is number of patch types (classes) present in the landscape, excluding the landscape border if present. SHEI measures the relative abundance of different patch types.</p>
Shannon's Diversity Index (SHDI)	$SHDI = - \sum_{i=1}^m (P_i \times \ln P_i)$ <p>P_i and m is the same as in SHEI. SHDI is a measure of land use/cover diversity in landscape.</p>
<i>Configurational</i>	
Edge density (ED)	$ED_i = \frac{\sum_{j=1}^n e_{ij}}{A}$ <p>e_{ij} is the total length of edges in the landscape for patch type (class) i and patch j, including landscape boundary and background segments involving patch type i. It measures the shape complexity for a patch type or the landscape.</p>
Patch density (PD)	$PD_i = n_i / A$ <p>n_i is the number of patches in the landscape for patch type (class) i. It is an index measuring spatial heterogeneity of the landscape.</p>
Landscape shape index (LSI)	$LSI_i = 0.25 \frac{\sum_{j=1}^n e_{ij}}{\sqrt{A}}$ <p>e_{ij} is the total length of edge for class i and patch j; $LSI \geq 1$, and increases as the shape of a patch becomes more irregular.</p>
Clumpiness index (CI)	$CI = \begin{cases} (G_i - P_i) / P_i & P_i > G_i \& P_i < 0.5 \\ (G_i - P_i) / (1 - P_i) & else \end{cases}$ <p>where</p> $G_i = g_{ii} / \left(\left(\sum_{k=1}^m g_{ik} \right) - \min e_i \right)$ <p>and g_{ii} is the number of like adjacencies (joins) between pixels of patch type (class) i based on the double-count method; g_{ik} is the number of adjacencies (joins) between pixels of patch types (classes) i and k based on the double-count method; $\min e_i$ is the minimum perimeter (in number of cell surfaces) of patch type (class) i for a maximally clumped class.</p>
Contagion (CONTAG)	$Contag = \left[\frac{\sum_{i=1}^m \sum_{k=1}^m \left[P_i \left(\frac{g_{ik}}{\sum_{k=1}^m g_{ik}} \right) \right] \times \left[\ln(P_i) \left(\frac{g_{ik}}{\sum_{k=1}^m g_{ik}} \right) \right]}{2 \ln(m)} \right] \times 100$ <p>where P_i is proportion of the landscape occupied by patch type (class) i; g_{ik} is the number of adjacencies (joins) between pixels of patch types (classes) i and k based on the double-count method; m is the number of patch types (classes) present in the landscape, including the landscape border if present. CONTAG describes the heterogeneity of a landscape.</p>

areas with high percent ISA. There was a strong linear relationship between LST and percent ISA based on regional mean values both in early spring and summer (Fig. 6-e, f). The linear relationship was much stronger in summer ($r^2 = 0.9843$) than early spring ($r^2 = 0.8545$). The data points were more scattered when percent ISA was low, and for the early spring.

To find out what caused these variations, we explored the thermal characteristics for different LCLU types by taking advantage of a high resolution LCLU map (2.5×2.5 m spatial resolution), which was generated based on air photos taken for the study area in 2000 in a separate study (Li et al., 2004). Due to the large volume of data, we performed the evaluation using the same 10×10 km sample area with

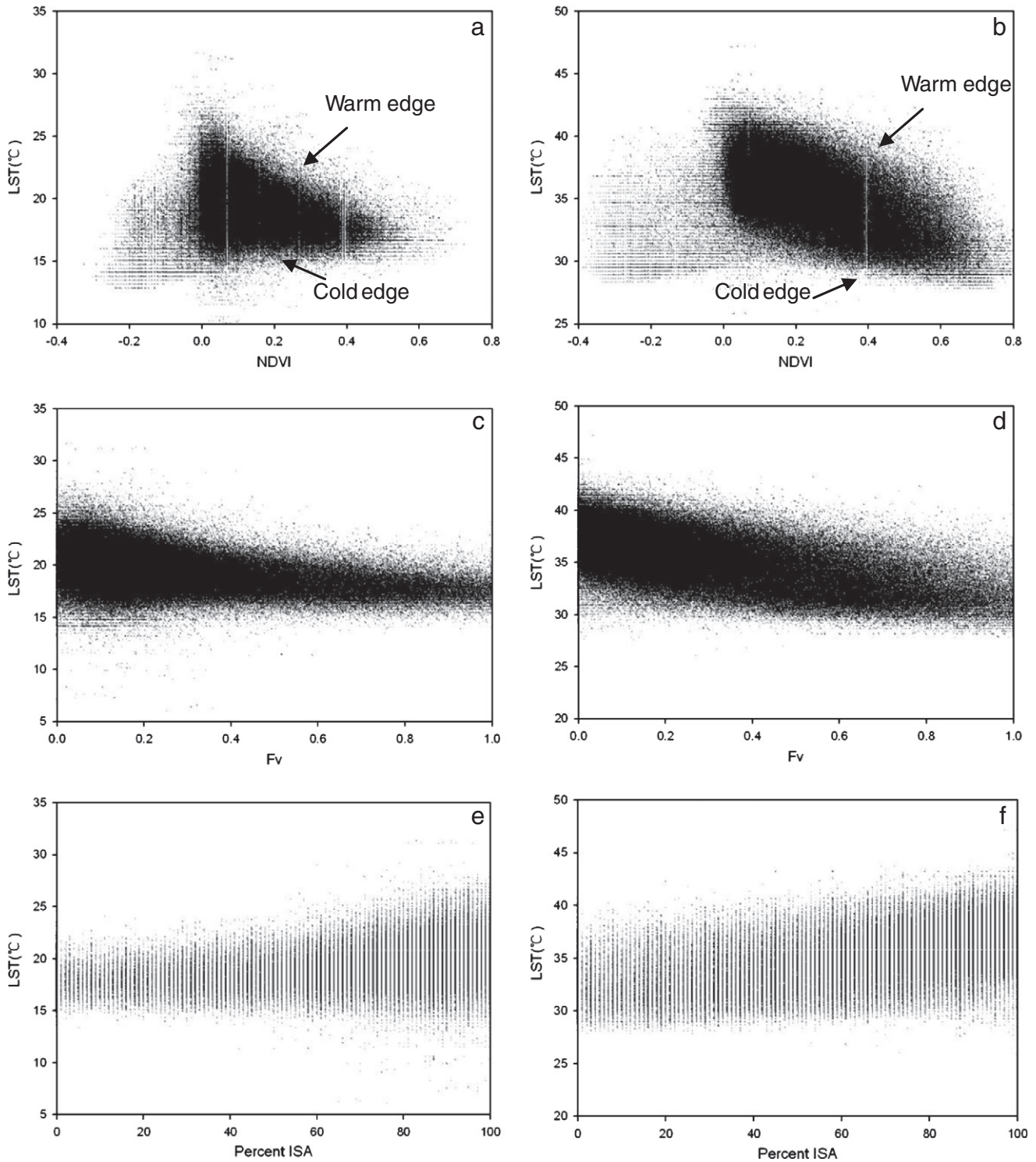


Fig. 5. Scattergrams of land surface temperature (LST) vs. normalized difference vegetation index (NDVI), fractional vegetation cover (Fv), and percent impervious surface area (ISA) at the pixel-by-pixel scale for the study area on two dates: a, c, and e: Mar. 13, 2001; b, d, and f: Jul. 3, 2001.

which we evaluated the landscape metrics, instead of the whole city. The sample area has presence of both high and low proportions of impervious surface. The shape of the scattergram between LST and percent ISA (not presented here) for the sample area was quite similar to that of the whole study area. The high spatial resolution LCLU map (Fig. 1-d) was superimposed upon the images of LST (Fig. 3 a, b) to extract LST for the corresponding LCLU types on a pixel by pixel basis

(at 2.5 m spatial resolution). The industrial land had the highest mean LST both in the summer (37.5 °C) and the early spring (20.7 °C) images. Direct heat release from industry may play a role here. It is interesting to note that the lowest mean LST was found in urban green (34.7 °C in summer and 19.1 °C in early spring) (Fig. 7), and water bodies had the second lowest mean LST in the highly dense urban area. Two factors may contribute to this temperature pattern:

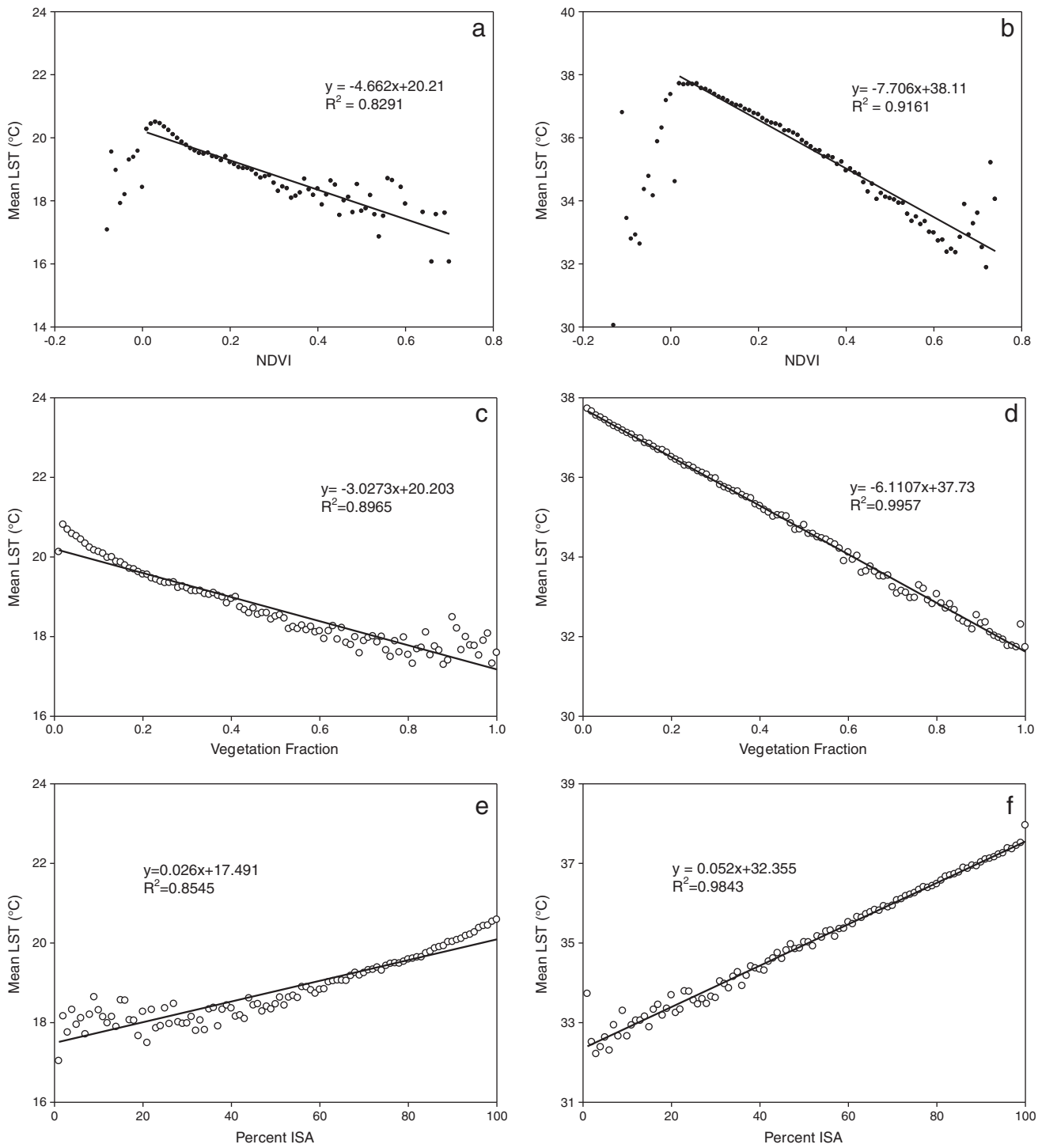


Fig. 6. Relationship of mean land surface temperature (LST) vs. normalized difference vegetation index (NDVI), Vegetation Fraction, and Percent ISA at the regional scale for the study area on two dates: a, c, and e: Mar. 13, 2001; b, d, and f: Jul. 3, 2001. Note only positive NDVI was used in the regression analysis between LST and NDVI.

(1) Water has the largest specific heat among all materials, thus slowest material to cool over night. At the midmorning satellite overpass, vegetated surface has not been heat up yet; (2) In the midmorning, a significant amount of urban green can be shaded by buildings, keeping its temperature low.

The larger standard deviations (SD) of LST were found to be associated with traffic (1.90 °C in summer and 1.96 °C in early spring) and industrial lands (1.71 °C in summer and 1.80 °C in early spring). The residential and public facility had a relatively small SD owing to their spatial homogeneity at the Landsat thermal image scale as they

usually are vegetated with trees and grass. Water bodies showed large SD, which might be caused by edge effects because the linear streams can be easily mixed with ambient urban environments in a pixel viewed by the thermal infrared sensor of the Thematic Mapper. Urban green-space showed low SD in early spring, but much higher SD in summer. Due to the height of the building in Shanghai, many street trees are shaded, resulting in low surface temperature, while non-shaded trees in the open urban areas have much higher surface temperature. The combined effect is high SD for surface temperature of urban green.

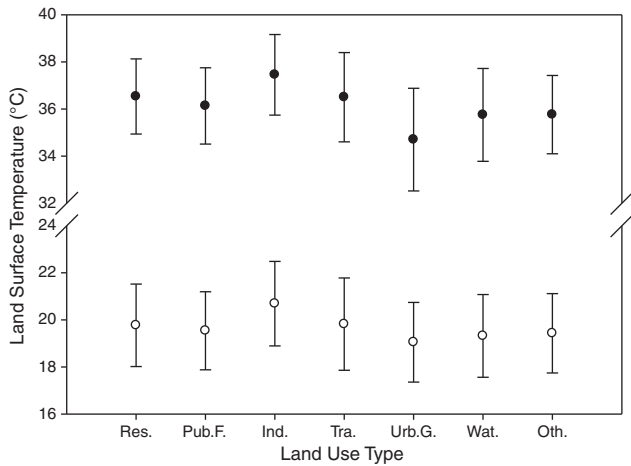


Fig. 7. Mean land surface temperature (LST) by land use types in sample plot (the error bar is one standard deviation of LST. The solid cycle is for Jul. 3, 2001, and the empty cycle is for Mar. 13, 2001).

We further explored the composition of LCLU types for areas with percent ISA exceeding 80%. We divide these pixels into three groups based on their surface temperature: those with LST greater than 1 SD from the mean (top group), those with LST within 1 SD around the mean (middle group), and those with LST 1 SD below the mean (bottom group). The pixel numbers of each LCLU type in the three groups were shown in Fig. 8. In the top group (Fig. 8-a, d), the residential land dominated the contribution to high LST, followed by industrial and traffic lands. In the middle (Fig. 8-b, e) and bottom (Fig. 8-c, f) groups, the residential land remains the dominant component in both summer and early spring, and dwarfed the presence of other land-cover and land-use types.

The residential land-use in the high resolution LCLU map was classified in detail based on its biophysical properties, i.e., their height and amount of vegetation. The composition of different types of residence for the three groups is shown in Fig. 9-a. Residence buildings with low vegetation presence primarily fall into the top group regardless the height of the building. The high and super-high rises primarily fall into the middle and bottom group, particularly those associated with relatively abundant vegetation (Fig. 9-b, c).

A closer look on the high resolution LCLU map revealed that residential and industrial lands with high LST mostly were those of blocks or communities and industrial-residential complex areas of high building density, such as textile mills, manufacturing factories, warehouses, and chemical plants which had dark tiles and asphalt rooftops but little vegetation. The residential and public facility lands with lower LST are mostly newly developed residential houses and universities or institutions with relatively lower building density and high vegetation cover.

3.3. The relationship between LST and urban landscape metrics

LST had a large range of variations at a given level of NDVI, percent vegetation, or ISA on a per-pixel basis (Fig. 5). One possible reason for this is the spatial configuration of land surface conditions. Correlation coefficients between LST and landscape metrics at both the class and landscape levels are given in Table 3. LST was highly correlated with landscape metrics for residential and urban green. For residential land, the mean LST was positively correlated to percent of land use (PLAND), edge density (ED), patch density (PD), and landscape shape index (LSI), but negatively correlated with clumpiness. For urban greenspace, the mean LST was negatively correlated with ED, PD, PLAND and LSI, and the negative correlation was much more

significant in the summer than in early spring. However, the correlation between LST with landscape metrics for residential land was stronger in early spring than that in summer. Among the landscape metrics analyzed, only PD was positively correlated with mean LST in the summer, while PLAND, ED and LSI were all significantly correlated with mean LST in the early spring images. Thus, the seasonal changes in vegetation pattern altered the spatial configuration of SUHI.

At the landscape level, the mean LST was negatively correlated with Shannon evenness index (SHEI) and positively correlated with landscape contagion (CONTAG) for both the summer and the early spring images (Table 4). All the other landscape pattern metrics were significantly correlated with mean LST for the early spring images, but not for the summer images although the signs of the correlation coefficients are consistent between summer and early spring images.

4. Discussion

4.1. Comparison of the correlation between different indicators and LST

The nonlinearity and seasonal variation in the LST-NDVI relationship make it challenging to predict LST from NDVI (Gillies and Carlson, 1995; Owen et al., 1998; Weng et al., 2004; Yuan and Bauer, 2007). Weng et al. (2004) proposed to use vegetation fraction in place of NDVI to evaluate the relationship between LST and vegetation. Our data also showed some minor improvement in the LST-Fv relationship (Fig. 5-c, d) over that of LST-NDVI on the pixel basis. The improvement was much clearer on the regional basis as is shown in Fig. 6-a-d that a much stronger statistical relationship exists between LST and Fv. Although Fv has a slightly stronger relationship with LST, it is highly related to NDVI (Carlson and Ripley, 1997; Carlson et al., 1995; Gutman and Ignatov, 1998), therefore, Fv suffers from the same limitations of variability and nonlinearity as NDVI to LST (Yuan and Bauer, 2007). However, when LST is related to positive NDVI only, the relationship between LST and NDVI is almost as strong as LST with Fv. When NDVI is negative, it is usually a mixture of several other no vegetation components, such as water, cloud, and sand. NDVI lost its physical meaning. It no longer reflects vegetation information. Thus analysis of NDVI with LST should only be limited to positive NDVI values. Given the complexity and uncertainty associated with SMA for Fv (Song, 2005; Wu and Murray, 2003). We believe NDVI should be preferred over vegetation fraction because NDVI is easy to obtain, and it does not suffer additional errors as Fv from SMA, such as selection of endmembers and endmember signature specification (Song, 2005) after the preprocessing is appropriately done.

Yuan and Bauer (2007) reported a strong linear relationship between LST and percent ISA based on regional mean values, and thus they recommended percent ISA as a complementary index to NDVI in surface urban heat island study. Our analysis found a similar strong linear relationship between LST and percent ISA at the regional scale. However, the relationship between LST and percent ISA is complex when examined on a pixel-by-pixel basis. Although impervious surfaces were frequently used as pseudo-invariant features in literature (Hall et al., 1991; Song et al., 2001; Schott et al., 1988) due to the insensitivity of spectral signatures to seasonal changes, there are significant percent ISA variation from the early spring to the summer images (Figs. 4-a, b and 5-e, f). The actual percent ISA may not change significantly from early spring to summer, but the viewable percent ISA decreases significantly due to increased vegetation cover from phenological change. Percent ISA is, therefore, not an invariant feature with season, and the expansion of tree crowns can obscure significant amount of ISA from view in remotely sensed images during the summer. As a result, there is a stronger relationship between LST and percent ISA at the regional scale for the summer image than that for the early spring image (Fig. 6-e, f).

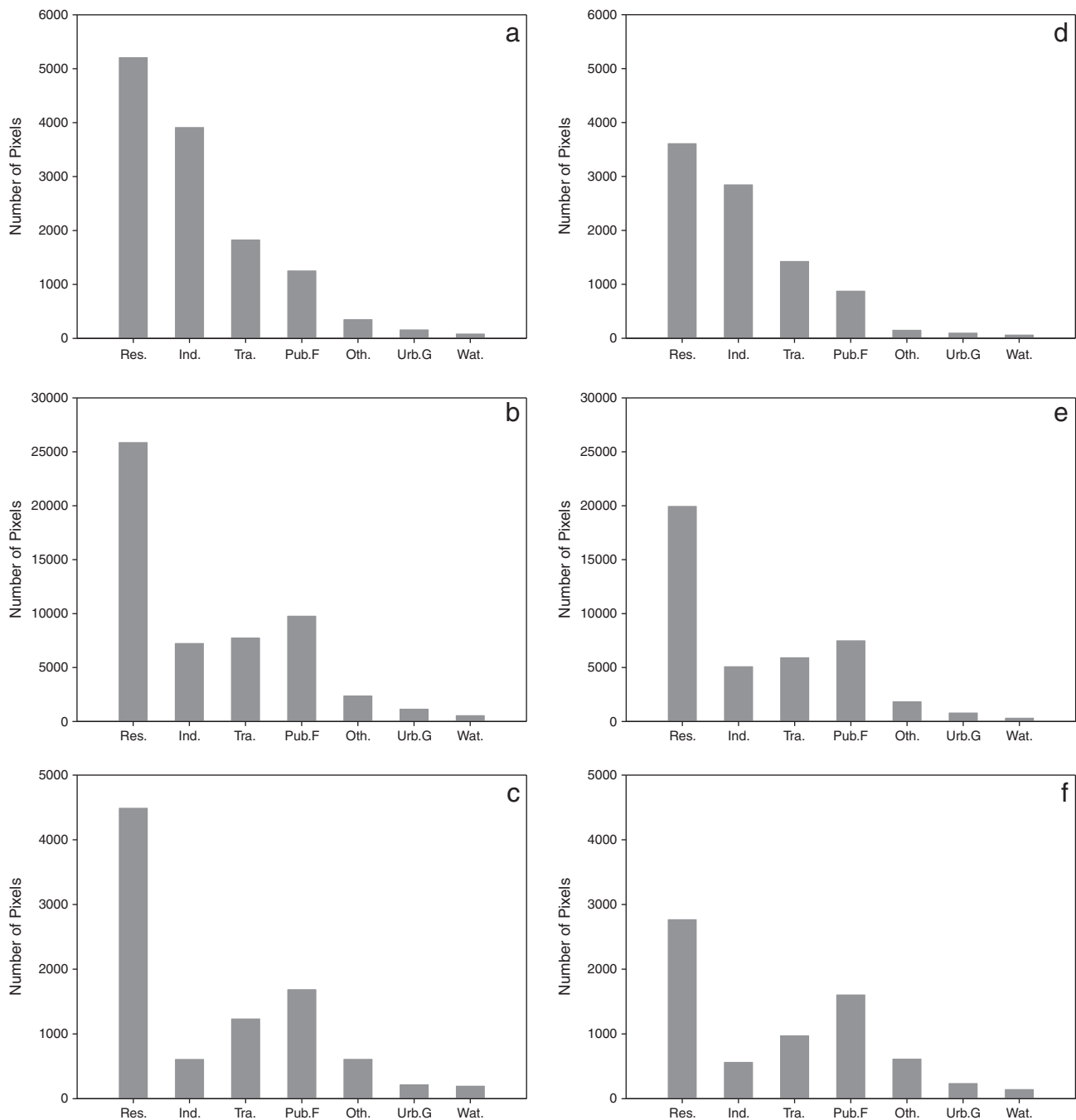


Fig. 8. Histogram of land use types in pixels with the percent ISA over 80% in the sample plot. These pixels were separated into three categories: top: pixels with temperatures one standard deviation above the mean (a: July 3, d: Mar 13, 2001), middle: pixels with temperatures within one standard deviation around the mean (b: July 3, e: Mar 13, 2001), and bottom: pixels with temperatures one standard deviation below the mean (c: July 3, f: Mar 13, 2001).

4.2. The influences of urban landscape structure on LST

On a pixel-by-pixel scale, LST not only depends on percent ISA, but also is strongly influenced by its spatial distribution (Table 3), its morphology, particularly height (Fig. 9) and land use (Fig. 8). Among the various types of impervious surfaces, industrial land use has the highest mean LST (Fig. 7). But it has a limited contribution to UHI due to the small spatial extent of industrial land use. Residential areas dominate the high percent ISA (>80%) areas (Fig. 8). The contribution of residential areas to LST strongly depends on its morphology. For high percent ISA areas, high rise residential areas have much lower LST than that for low rise residential areas due to several reasons. First, there is a greater portion of horizontal active surface in low rise

residential areas than that in the high rise. Horizontal active surface is what the satellite view on the ground with nadir viewing sensors like Landsat (Nichol, 1994; Roth et al., 1989). Second, smaller buildings with lower building mass have lower thermal inertia, and cast shorter shadows, and vice versa for high rises (Nichol, 1996, 1998). Third, the aerodynamics for low rise and high buildings are significantly different in the lower boundary layer as wind speed increases with height. Thus, there is a higher aerodynamic conductance to carry the heat away from the surface on high rise buildings than that for the low rise. Lastly, in the lower boundary layer, air temperature decreases with height. The air temperature is lower at the top of the high rise than that of the low rise. Vegetation further complicates the situation. Low rise low vegetation impervious surface dominates the high

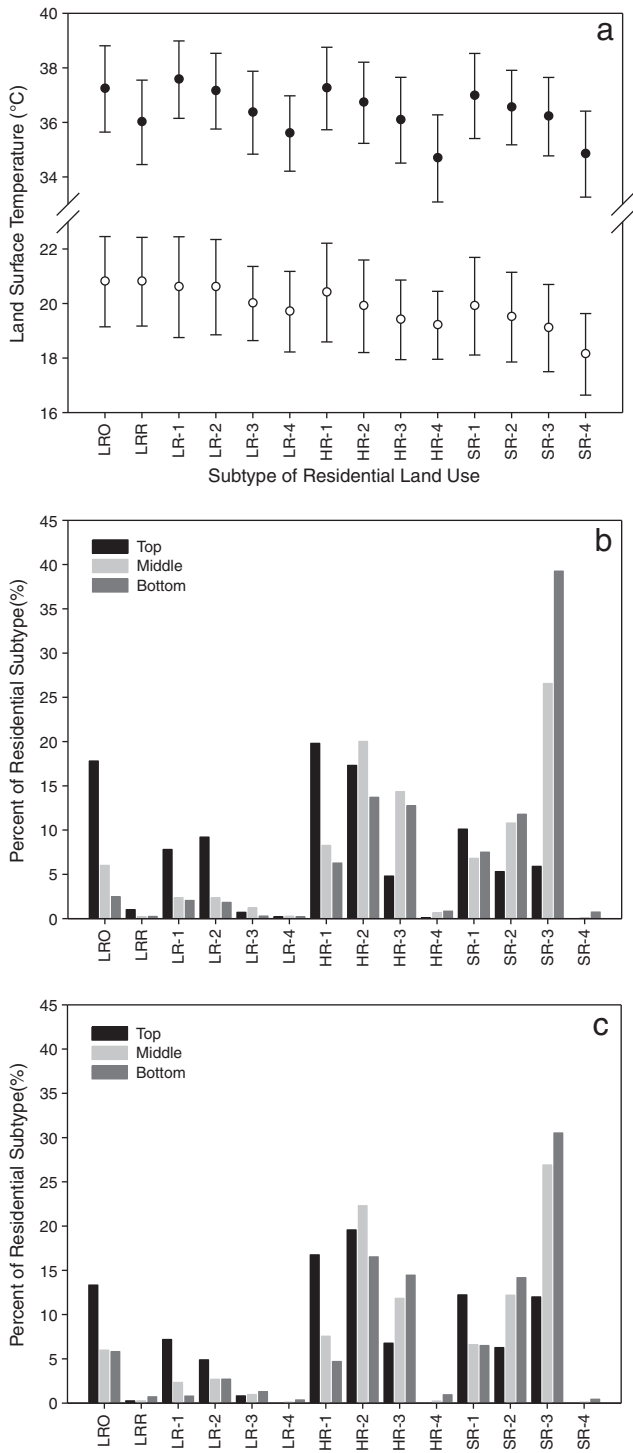


Fig. 9. Mean LST corresponding to subtypes of residential land use in sample plot. LRO: Low-rising old and humble house with green cover less than 10%; LRR: Low-rising rural house (less than 3 stories); LR-1: Low-rising house (less than 7 stories) with green cover less than 10%, LR-2: Low-rising house with green cover between 10 and 30%, LR-3: Low-rising house with green cover between 30 and 50%, LR-4: Low-rising house with green cover over 50%; HR-1: High-rising house (7–18 stories) with green cover less than 10%, HR-2: High-rising house with green cover between 10 and 30%, HR-3: High-rising house with green cover between 30 and 50%, HR-4: High-rising house with green cover over 50%; SR-1: Superhigh-rising house (over 18 stories) with green cover less than 10%, SR-2: Superhigh-rising house with green cover between 10 and 30%, SR-3: Superhigh-rising house with green cover between 30 and 50%, SR-4: Superhigh-rising house with green cover over 50%. The error bar is one standard deviation. Solid cycle for Jul. 3, 2001; empty cycle for Mar. 13, 2001 (a for all residential subtypes, b for three subgroups with %ISA ≥ 80% Mar. 13, 2001, and c for three subgroups with %ISA ≥ 80% Jul. 3, 2001).

Table 3

Pearson correlation coefficients between land surface temperature and class-level landscape pattern metrics.

Land use class	Image date	PLAND	PD	ED	LSI	CLUMPY
Residential	Mar. 13	.425*	.557**	.569**	.501*	-.585**
	Jul. 03	.306	.460*	.416*	.361	-.439*
Public facility	Mar. 13	-.264	.168	-.013	.160	-.286
	Jul. 03	-.496*	-.020	-.240	-.045	-.134
Industrial	Mar. 13	-.078	.016	-.067	.008	-.322
	Jul. 03	.185	.185	.181	.161	-.145
Traffic	Mar. 13	.414*	.247	.501*	.424*	-.301
	Jul. 03	.311	.529**	.388	.339	-.277
Urban green	Mar. 13	-.356	-.335	-.402*	-.318	-.019
	Jul. 03	-.380	-.602**	-.570**	-.545**	.188
Water	Mar. 13	-.177	.029	.045	.027	.102
	Jul. 03	.104	-.136	.147	.070	.192
The other	Mar. 13	-.441*	-.150	-.358	-.096	-.403*
	Jul. 03	-.628**	-.316	-.554**	-.294	-.303

* Correlation is significant at the 0.05 level (2-tailed).

** Correlation is significant at the 0.01 level (2-tailed).

impervious surface LST, but high vegetation presence can significantly mitigate the LST for high density low rise residential areas (Fig. 9).

Previous studies on UHI focused primarily on the relationship between LST and land cover composition (Chen et al., 2006; Nichol, 1996, 1998; Roth et al., 1989; Weng, 2001; Weng et al., 2006, 2004). Our study found that urban LST is not only influenced by land cover composition but also its spatial configuration. LST is correlated with various landscape pattern metrics (Tables 3 and 4). LST is generally negatively correlated with clumpiness at the pixel-by-pixel scale (Table 3), and Shannon's diversity index at the landscape scale (Table 4), indicating a mixture of impervious surface with other land cover types reduces SUHI effect. Only the LST of industrial land use was not correlated with any of the landscape pattern metrics, which probably was because of its small spatial extent.

4.3. Implications for urban planning and land use management

The relationships between LST and urban landscape metrics have important implications for urban planning and land use management to mitigate the urban heat islands. Urbanization has resulted in complex urban landscapes (Luck and Wu, 2002; Weng, 2007; Yu and Ng, 2007) with impervious surface as the primary feature. Although previous studies (Chen et al., 2006; Lu and Weng, 2006; Weng, 2001; Weng et al., 2004) and ours found that impervious surface contributes greatly to surface urban heat islands, our research revealed that we can mitigate such effect by altering the composition and spatial configuration of land use at class and landscape level, respectively. At the class level, all landscape metric measurements for residential land use are significantly related to LST, and mostly positively related except clumpiness index (CLUMPY), and nearly all landscape metric measurements are negatively correlated with LST. Special attention should be paid to these two land use for urban planning. Even if we may not be able to reduce the proportion of ISA in cities where the land resource is valuable and scarce such as in Shanghai, we still can mitigate LST by increasing building height and limiting building density and extent.

Table 4

Pearson correlation coefficients between land surface temperature and landscape-level pattern metrics.

Image date	PD	ED	LSI	CONTAG	SHDI	SHEI
03 Jul., 2001	.257	.298	.299	.559**	-.335	-.547**
13 Mar., 2001	.413*	.455*	.455*	.614**	-.538**	-.645**

* Correlation is significant at the 0.05 level (2-tailed).

** Correlation is significant at the 0.01 level (2-tailed).

Urban greenspace is always beneficial to mitigating urban heat islands. It is well known that the size of urban greenspace is an important factor influencing its cooling effect (Chang et al., 2007; Jauregui, 1990; Lee et al., 2009). Their spatial arrangement may affect the cooling effect of greenspace as well (Chang et al., 2007). Our results show that, at the landscape scale, LST is positively related to the area (PLAND), shape (ED, LSI), and density (PD), these indices primarily reflect the configuration for ISA in Shanghai. However, LST is negatively related to SHDI and SHEI, indicating a blending of different land use helps mitigate SUHI. These results indicate that interspersing greenspace into urban patches has a stronger mitigation effect than its concentrated form.

5. Conclusions

Both the composition and configuration of urban landscape significantly influence SUHI in the city of Shanghai, China. Vegetation mitigates SUHI, while ISA strengthens it. Residential land use is the primary contributor to SUHI, followed by industrial land use. Among the residential land uses, areas with low to mid-rise buildings with low vegetation cover result in strong UHI effects. At the landscape scale, the spatial configuration of residential, urban greenspace, and public facility is strongly correlated with LST. All the spatial pattern metrics are significantly correlated to LST at the regional scale for the early spring image, but only CONTAG and SHEI are significantly correlated with LST for the summer images, indicating strong effects of vegetation on the spatial configuration of other components. Our findings have important implications for urban planning to mitigate UHI effects. Given the same percentage of urban green area, it is more effective to reduce the effects of SUHI when it is distributed across the urban landscape than when it is concentrated. Given the same percent ISA, there would be less SUHI effect when it is more spatially distributed. High density low-rise residential areas with low vegetation cover should be avoided in urban planning.

Acknowledgments

This research has been supported by grants from National Natural Science Foundation of China (No. 30770384) and the Ministry of Education of China (No. 106079) to J. Li, partially supported by the Shanghai Priority Academic Discipline and the State's 10th 5-year "211 Project"-supported key academic discipline program of East China Normal University. We are grateful to Shanghai City Development and Information Center for providing aerial photos. We also thank Yujie Wang, Tong Wu, Ying Zhu, Chen Meng, Sanping Gao, Mingce Xu, Rong li, Cheng Li, and Hai Qing for their assistance with the digitization of aerial photos. The helpful comments and suggestions from the four anonymous reviewers are very gratefully acknowledged.

References

- Alberti, M. (2005). The effects of urban patterns on ecosystem function. *International Regional Science Review*, 28(2), 168–192.
- Artis, D. A., & Carnahan, W. H. (1982). Survey of emissivity variability in thermography of urban areas. *Remote Sensing of Environment*, 12(4), 313–329.
- Balling, R. C. J., & Brazel, S. W. (1988). High-resolution surface temperature patterns in a complex urban terrain. *Photogrammetric Engineering and Remote Sensing*, 54(9), 1289–1293.
- Barsi, J. A., Schott, J. R., Palluconi, F. D., Helder, D. L., Hook, S. J., Markham, B. L., et al. (2003). Landsat TM and ETM+ thermal band calibration. *Canadian Journal of Remote Sensing*, 29(2), 141–153.
- Buyantuyev, A., & Wu, J. (2010). Urban heat islands and landscape heterogeneity: Linking spatiotemporal variations in surface temperatures to land-cover and socioeconomic patterns. *Landscape Ecology*, 25(1), 17–33.
- Carlson, T. N., Capehart, W. J., & Gillies, R. R. (1995). A new look at the simplified method for remote sensing of daily evapotranspiration. *Remote Sensing of Environment*, 54(2), 161–167.
- Carlson, T. N., Gillies, R. R., & Perry, E. M. (1994). A method to make use of thermal infrared temperature and NDVI measurements to infer surface soil water content and fractional vegetation cover. *Remote Sensing Reviews*, 9(1), 161–173.
- Carlson, T. N., & Ripley, D. A. (1997). On the relation between NDVI, fractional vegetation cover, and leaf area index. *Remote Sensing of Environment*, 62(3), 241–252.
- Carlson, T. N., & Traci Arthur, S. (2000). The impact of land use – land cover changes due to urbanization on surface microclimate and hydrology: A satellite perspective. *Global and Planetary Change*, 25(1–2), 49–65.
- Chander, G., & Groeneveld, D. P. (2009). Intra-annual NDVI validation of the Landsat 5 TM radiometric calibration. *International Journal of Remote Sensing*, 30(6), 1621–1628.
- Chander, G., & Markham, B. (2003). Revised Landsat-5 TM radiometric calibration procedures and postcalibration dynamic ranges. *IEEE Transactions on Geoscience and Remote Sensing*, 41(11), 2674–2677.
- Chander, G., Markham, B. L., & Helder, D. L. (2009). Summary of current radiometric calibration coefficients for Landsat MSS, TM, ETM+, and EO-1 ALI sensors. *Remote Sensing of Environment*, 113(5), 893–903.
- Chang, C. -R., Li, M. -H., & Chang, S. -D. (2007). A preliminary study on the local cool-island intensity of Taipei city parks. *Landscape and Urban Planning*, 80(4), 386–395.
- Chen, X. -L., Zhao, H. -M., Li, P. -X., & Yin, Z. -Y. (2006). Remote sensing image-based analysis of the relationship between urban heat island and land use/cover changes. *Remote Sensing of Environment*, 104(2), 133–146.
- Cheval, S., & Dumitrescu, A. (2009). The July urban heat island of Bucharest as derived from modis images. *Theoretical and Applied Climatology*, 96(1), 145–153.
- Civco, D. L., Hurd, J. D., Arnold, C. L., & Prisløe, S. (2002). Characterization of suburban sprawl and forest fragmentation through remote sensing applications. *Proceedings of the ASPRS 2000 Annual Convention*.
- Deguchi, C., & Sugio, S. (1994). Estimations for percent impervious area by the use of satellite remote sensing imagery. *Water Science and Technology*, 29(1–2), 135–144.
- Gallo, K. P., McNab, A. L., Karl, T. R., Brown, J. F., Hood, J. J., & Tarpley, J. D. (1993). The use of NOAA AVHRR data for assessment of the urban heat island effect. *Journal of Applied Meteorology*, 32(5), 899–908.
- Gillespie, A., Rokugawa, S., Matsunaga, T., Cothren, J. S., Hook, S., & Kahle, A. B. (1998). A temperature and emissivity separation algorithm for Advanced Spaceborne Thermal Emission and Reflection Radiometer (ASTER) images. *IEEE Transactions on Geoscience and Remote Sensing*, 36(4), 1113–1126.
- Gillies, R. R., & Carlson, T. N. (1995). Thermal remote sensing of surface soil water content with partial vegetation cover for incorporation into climate models. *Journal of Applied Meteorology*, 34(4), 745–756.
- Gillies, R. R., Kustas, W. P., & Humes, K. S. (1997). A verification of the 'triangle' method for obtaining surface soil water content and energy fluxes from remote measurements of the Normalized Difference Vegetation Index (NDVI) and surface radiant temperature. *International Journal of Remote Sensing*, 18(15), 3145–3166.
- Goetz, S. J., Wright, R. K., Smith, A. J., Zinecker, E., & Schaub, E. (2003). IKONOS imagery for resource management: Tree cover, impervious surfaces, and riparian buffer analyses in the mid-Atlantic region. *Remote Sensing of Environment*, 88(1–2), 195–208.
- Goward, S. N., Xue, Y., & Czajkowski, K. P. (2002). Evaluating land surface moisture conditions from the remotely sensed temperature/vegetation index measurements: An exploration with the simplified simple biosphere model. *Remote Sensing of Environment*, 79(2–3), 225–242.
- Gustafson, E. J. (1998). Minireview: Quantifying landscape spatial pattern: What is the state of the art? *Ecosystems*, 1(2), 143–156.
- Gutman, G., & Ignatov, A. (1998). The derivation of the green vegetation fraction from NOAA/AVHRR data for use in numerical weather prediction models. *International Journal of Remote Sensing*, 19(8), 1533–1543.
- Hall, F. G., Strebel, D. E., Nickeson, J. E., & Goetz, S. J. (1991). Radiometric rectification: Toward a common radiometric response among multitemporal, multisensor images. *Remote Sensing of Environment*, 35(1), 11–27.
- Herold, M., Goldstein, N. C., & Clarke, K. C. (2003). The spatiotemporal form of urban growth: Measurement, analysis and modeling. *Remote Sensing of Environment*, 86(3), 286–302.
- Herold, M., Scepan, J., & Clarke, K. C. (2002). The use of remote sensing and landscape metrics to describe structures and changes in urban land uses. *Environment and Planning A*, 34(8), 1443–1458.
- Hodgson, M. E., Jensen, J. R., Tullis, J. A., Riordan, K. D., & Archer, C. M. (2003). Synergistic use of lidar and color aerial photography for mapping urban parcel imperviousness. *Photogrammetric Engineering & Remote Sensing*, 69(9), 73–980.
- Hu, X., & Weng, Q. (2009). Estimating impervious surfaces from medium spatial resolution imagery using the self-organizing map and multi-layer perceptron neural networks. *Remote Sensing of Environment*, 113(10), 2089–2102.
- Jauregui, E. (1990). Influence of a large urban park on temperature and convective precipitation in a tropical city. *Energy and Buildings*, 15(3–4), 457–463.
- Ji, M., & Jensen, J. R. (1999). Effectiveness of subpixel analysis in detecting and quantifying urban imperviousness from Landsat thematic mapper imagery. *Geocarto International*, 14(4), 33–41.
- Lee, S. -H., Lee, K. -S., Jin, W. -C., & Song, H. -K. (2009). Effect of an urban park on air temperature differences in a central business district area. *Landscape and Ecological Engineering*, 5(2), 183–191.
- Li, H., & Reynolds, J. F. (1993). A new contagion index to quantify spatial patterns of landscapes. *Landscape Ecology*, 8(3), 155–162.
- Li, H., & Wu, J. (2004). Use and misuse of landscape indices. *Landscape Ecology*, 19(4), 389–399.
- Li, J., Wang, Y., Shen, X., & Song, Y. (2004). Landscape pattern analysis along an urban-rural gradient in the Shanghai metropolitan region. *Acta Ecologica Sinica*, 24(9), 1973–1980.
- Liu, H., & Weng, Q. (2008). Seasonal variations in the relationship between landscape pattern and land surface temperature in Indianapolis, USA. *Environmental Monitoring and Assessment*, 144(1), 199–219.

- Lo, C. P., Quattrochi, D. A., & Luvall, J. C. (1997). Application of high-resolution thermal infrared remote sensing and GIS to assess the urban heat island effect. *International Journal of Remote Sensing*, 18(2), 287–304.
- Lu, D., & Weng, Q. (2006). Spectral mixture analysis of ASTER images for examining the relationship between urban thermal features and biophysical descriptors in Indianapolis, Indiana, USA. *Remote Sensing of Environment*, 104(2), 157–167.
- Luck, M., & Wu, J. (2002). A gradient analysis of urban landscape pattern: A case study from the Phoenix metropolitan region, Arizona, USA. *Landscape Ecology*, 17(4), 327–339.
- Markham, B. L., & Barker, J. L. (1985). Spectral characterization of the LANDSAT thematic mapper sensors. *International Journal of Remote Sensing*, 6(5), 697–716.
- McGarigal, K., Cushman, S. A., Neel, M. C., & Ene, E. (2002). FRAGSTATS: Spatial pattern analysis program for categorical maps. Computer software program produced by the authors at the University of Massachusetts, Amherst Available at the following web site. www.umass.edu/landeco/research/fragstats/fragstats.html
- McGarigal, K., & Marks, B. J. (1995). FRAGSTATS: spatial pattern analysis program for quantifying landscape structure. *Gen. Tech. Rep. PNW-CR-351*. (pp. 122)Portland, OR: U.S. Department of Agriculture, Forest Service, Pacific Northwest Research Station.
- Nichol, J. E. (1994). A GIS-based approach to microclimate monitoring in Singapore's high-rise housing estates. *Photogrammetric Engineering and Remote Sensing*, 60(10), 1225–1232.
- Nichol, J. E. (1996). High-resolution surface temperature patterns related to urban morphology in a tropical city: A satellite-based study. *Journal of Applied Meteorology*, 35(1), 135–146.
- Nichol, J. E. (1998). Visualisation of urban surface temperatures derived from satellite images. *International Journal of Remote Sensing*, 19(9), 1639–1649.
- Nichol, J. (2009). An emissivity modulation method for spatial enhancement of thermal satellite images in urban heat island analysis. *Photogrammetric Engineering and Remote Sensing*, 75(5), 547–556.
- O'Neill, R. V., Krummel, J. R., Gardner, R. H., Sugihara, G., Jackson, B., DeAngelis, D. L., et al. (1988). Indices of landscape pattern. *Landscape Ecology*, 1(3), 153–162.
- Owen, T. W., Carlson, T. N., & Gillies, R. R. (1998). An assessment of satellite remotely-sensed land cover parameters in quantitatively describing the climatic effect of urbanization. *International Journal of Remote Sensing*, 19(9), 1663–1681.
- Phinn, S., Stanford, M., Scarth, P., Murray, A. T., & Shyy, P. T. (2002). Monitoring the composition of urban environments based on the vegetation-impervious surface-soil (VIS) model by subpixel analysis techniques. *International Journal of Remote Sensing*, 23(20), 4131–4153.
- Ridd, M. K. (1995). Exploring a V-I-S (vegetation-impervious surface-soil) model for urban ecosystem analysis through remote sensing: Comparative anatomy for cities. *International Journal of Remote Sensing*, 16(12), 2165–2185.
- Roth, M., Oke, T. R., & Emery, W. J. (1989). Satellite derived urban heat islands from three coastal cities and the utilisation of such data in urban climatology. *International Journal of Remote Sensing*, 10(11), 1699–1720.
- Sandholt, I., Rasmussen, K., & Andersen, J. (2002). A simple interpretation of the surface temperature/vegetation index space for assessment of surface moisture status. *Remote Sensing of Environment*, 79(2–3), 213–224.
- Schott, J. R., Salvaggio, C., & Volchok, W. J. (1988). Radiometric scene normalization using pseudoinvariant features. *Remote Sensing of Environment*, 26(1), 1–14 IN11, 15–16.
- Small, C. (2001). Estimation of urban vegetation abundance by spectral mixture analysis. *International Journal of Remote Sensing*, 22(7), 1305–1334.
- Shanghai Municipal Statistics Bureau. (2006). *Shanghai statistical yearbook 2006*. Beijing: China Statistics Press.
- Snyder, W. C., Wan, Z., Zhang, Y., & Feng, Y. Z. (1998). Classification-based emissivity for land surface temperature measurement from space. *International Journal of Remote Sensing*, 19(14), 2753–2774.
- Sobrino, J. A., Caselles, V., & Becker, F. (1990). Significance of the remotely sensed thermal infrared measurements obtained over a citrus orchard. *ISPRS Journal of Photogrammetry and Remote Sensing*, 44(6), 343–354.
- Sobrino, J. A., Jiménez-Muñoz, J. C., & Paolini, L. (2004). Land surface temperature retrieval from LANDSAT TM 5. *Remote Sensing of Environment*, 90(4), 434–440.
- Song, C. (2004). Cross-sensor calibration between Ikonos and Landsat ETM+ for spectral mixture analysis. *IEEE Geoscience and Remote Sensing Letters*, 1(4), 272–276.
- Song, C. (2005). Spectral mixture analysis for subpixel vegetation fractions in the urban environment: How to incorporate endmember variability? *Remote Sensing of Environment*, 95(2), 248–263.
- Song, C., Woodcock, C. E., Seto, K. C., Lenney, M. P., & Macomber, S. A. (2001). Classification and change detection using Landsat TM data: When and how to correct atmospheric effects? *Remote Sensing of Environment*, 75(2), 230–244.
- Streutker, D. R. (2002). A remote sensing study of the urban heat island of Houston, Texas. *International Journal of Remote Sensing*, 23(13), 2595–2608.
- Streutker, D. R. (2003). Satellite-measured growth of the urban heat island of Houston, Texas. *Remote Sensing of Environment*, 85(3), 282–289.
- Tran, H., Uchihama, D., Ochi, S., & Yasuoka, Y. (2006). Assessment with satellite data of the urban heat island effects in Asian mega cities. *International Journal of Applied Earth Observation and Geoinformation*, 8(1), 34–48.
- Turner, M. G. (2005). Landscape ecology: What is the state of the science? *Annual Review of Ecology, Evolution, and Systematics*, 36(1), 319–344.
- Turner, M. G., & Gardner, R. H. (1991). *Quantitative methods in landscape ecology: The analysis and interpretation of landscape heterogeneity*. New York, USA: Springer-Verlag.
- United Nations. (2008). *World urbanization prospects: The 2007 revision*. New York.
- Voogt, J. A. (2002). Urban heat island. In I. Douglas (Ed.), *Causes and consequences of global environmental change*, Vol. 3. (pp. 660–666)Chichester: John Wiley & Sons, Ltd.
- Voogt, J. A., & Oke, T. R. (2003). Thermal remote sensing of urban climates. *Remote Sensing of Environment*, 86(3), 370–384.
- Weng, Q. (2001). A remote sensing-GIS evaluation of urban expansion and its impact on surface temperature in the Zhujiang Delta, China. *International Journal of Remote Sensing*, 22(10), 1999–2014.
- Weng, Y. -C. (2007). Spatiotemporal changes of landscape pattern in response to urbanization. *Landscape and Urban Planning*, 81(4), 341–353.
- Weng, Q., Liu, H., & Lu, D. (2007). Assessing the effects of land use and land cover patterns on thermal conditions using landscape metrics in city of Indianapolis, United States. *Urban Ecosystems*, 10(2), 203–219.
- Weng, Q., Lu, D., & Liang, B. (2006). Urban surface biophysical descriptors and land surface temperature variations. *Photogrammetric Engineering & Remote Sensing*, 72(11), 1275–1286.
- Weng, Q., Lu, D., & Schubring, J. (2004). Estimation of land surface temperature-vegetation abundance relationship for urban heat island studies. *Remote Sensing of Environment*, 89(4), 467–483.
- Weng, Q., & Quattrochi, D. A. (2006). Thermal remote sensing of urban areas: An introduction to the special issue. *Remote Sensing of Environment*, 104(2), 119–122.
- Woodcock, C. E., & Strahler, A. H. (1987). The factor of scale in remote sensing. *Remote Sensing of Environment*, 21(3), 311–332.
- Wu, C. (2004). Normalized spectral mixture analysis for monitoring urban composition using ETM+ imagery. *Remote Sensing of Environment*, 93(4), 480–492.
- Wu, C., & Murray, A. T. (2003). Estimating impervious surface distribution by spectral mixture analysis. *Remote Sensing of Environment*, 84(4), 493–505.
- Wu, J. (2000). *Landscape ecology: Pattern, process, scale and hierarchy*. China, Beijing: Higher Education Press.
- Wu, J. (2008). Making the case for landscape ecology: An effective approach to urban sustainability. *Landscape Journal*, 27(1), 41–50.
- Wu, J., Shen, W., Sun, W., & Tueller, P. T. (2002). Empirical patterns of the effects of changing scale on landscape metrics. *Landscape Ecology*, 17(8), 761–782.
- Wu, J., Jenerette, G. D., Buyantuyev, A., & Redman, C. L. (2011). Quantifying spatiotemporal patterns of urbanization: The case of the two fastest growing metropolitan regions in the United States. *Ecological Complexity*, 8(1), 1–8.
- Xian, G., & Crane, M. (2006). An analysis of urban thermal characteristics and associated land cover in Tampa Bay and Las Vegas using Landsat satellite data. *Remote Sensing of Environment*, 104(2), 147–156.
- Yang, L., Huang, C., Homer, C. G., Wylie, B. K., & Coan, M. J. (2003). An approach for mapping large-area impervious surfaces: Synergistic use of Landsat-7 ETM+ and high spatial resolution imagery. *Canadian Journal of Remote Sensing*, 29(2), 230–240.
- Yang, X., & Liu, Z. (2005). Use of satellite-derived landscape imperviousness index to characterize urban spatial growth. *Computers, Environment and Urban Systems*, 29(5), 524–540.
- Yu, X. J., & Ng, C. N. (2007). Spatial and temporal dynamics of urban sprawl along two urban-rural transects: A case study of Guangzhou, China. *Landscape and Urban Planning*, 79(1), 96–109.
- Yuan, F., & Bauer, M. E. (2007). Comparison of impervious surface area and normalized difference vegetation index as indicators of surface urban heat island effects in Landsat imagery. *Remote Sensing of Environment*, 106(3), 375–386.